MDPI

Article

Crystallographic Characteristics of Inorganic Mineral in Mammoth Ivory and Ivory

Xueying Sun [1], Mingyue He [1,*] and Jinlin Wu [1,2]

1   School of Gemology, China University of Geosciences, Beijing 100083, China;
    Sunxyforever@outlook.com (X.S.); wujl@ngtc.com.cn (J.W.)
2   National Gemstone Testing Center Shenzhen Laboratory, Shenzhen 518020, China
*   Correspondence: hemy@cugb.edu.cn

Abstract: In this paper, the chemical composition and crystalline properties of mammoth ivory and ivory were systematically analyzed. The results revealed that the microscopic crystalline hydroxyapatites are the major component of minerals in mammoth ivory and ivory. The Ca/P ratios of the samples studied are obviously lower than apatite. Refined cell parameters showed a similar value between mammoth ivory (a = 9.4148 Å and b = 6.8821 Å) and ivory (a = 9.4166 Å and c = 6.8841 Å). Individual crystal sizes in mammoth ivory and ivory are estimated to be 20.41–23.16 and 18.92–21.50 nm, respectively. The calculated crystallinity of two kinds of ivory (mammoth ivory: 1.55; ivory: 1.4) is far lower than geological mineral fluorapatite due to the impact of tissue function and organic matrix.

Keywords: crystallographic characteristics; hydroxyapatite; mammoth ivory; ivory

1. Introduction

Research of biomineralization has had a long history, the understanding of which is advanced by analyzing the function of living beings and organic evolution in mineralization [1–3]. Micro-structured biomaterials such as bone and teeth have gradually received much more attention. Tabular hydroxyapatite, which sets up the skeleton of vertebrates, offers significant hardness and supports the whole body, is the typical material from biomineralization [3–5]. The impact of the organic materials during bio-mineralization leads to some excellent properties, for example, a periodic layer composed of hydroxyapatite inhibits new cracks and reduces the energy transferred across both layers, even reflecting some of the incident energy [6,7].

Significant progress has been made on the bones and teeth of several species using electron microscopy. Robinson firstly discovered that the tabular hydroxyapatite in human bone was distributed along the c-axis of collagen triple helixes with the size of $50 \times 25 \times 10$ nm, which also confirmed that the nano-hydroxyapatite can be observed [8]. Previous literature revealed that the hydroxyapatite crystal size has generally been accepted to be 35–70 nm in length, with a width of approximately 25–50 nm and a minimum uniform thickness of 2–5 nm [8–11]. Such crystal sizes present a conceptual problem related to the ultrastructure accommodation at the molecular level in collagen. The crystals are inferred to be located within or between the collagen fibrils [1,12,13]. The hydroxyapatite in bone and teeth is calcium deficient and carbonated. With age, its crystallinity decreased but the carbonate content increased. In addition, the effect of calcium and phosphate in demineralization and remineralization dynamics has been explained [14].

In many respects, mammoth ivory resembles bone and teeth in the organic and inorganic matrix compositions. The hierarchical structure of ivory, including the spatial relationship between apatite crystals and collagen fibrils, can be recognized [15,16]. The existence of a preferred orientation of hydroxyapatite in ivory and mammoth ivory was verified [17]. The average sizes of the crystals in ivory were measured to be 31 nm in length, 20 nm in width, and 3 nm in thickness, which is smaller than bone [18]. These phenomena

present unique opportunities for the study of crystalline characteristics of hydroxyapatite in mammoth ivory and ivory from an elephant.

Due to the lack of research on mammoth ivory, crystalline characteristics of hydroxyapatite in mammoth ivory and ivory from an elephant are analyzed in this study applying X-ray diffraction (XRD), energy dispersive spectroscopy (EDS), and infrared spectroscopy (IR). The significance of this finding not only applies to the bio-mineral structure but also provides a kind of new theoretic basis for further study into the process of biological mineralization and a useful reference for synthesizing nano-hydroxyapatite with excellent properties [19].

2. Materials and Methods

2.1. Materials

In this study, three specimens were collected: (i) a sample of mammoth ivory (MI) from mammoth, recovered from tundra in the region of Siberia, Russia; (ii) a sample of ivory (I) originating from adult Zimbabwean elephants; and (iii) a sample of fluorapatite (F), used as standard material (Figure 1).
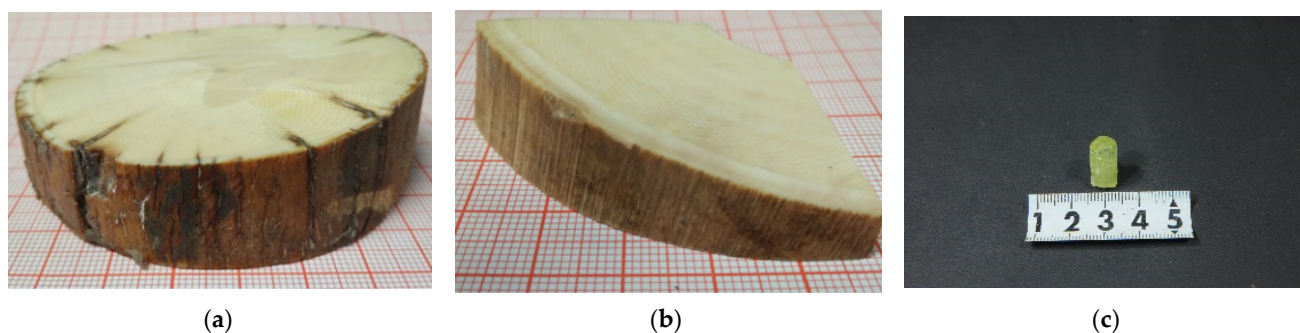

(a)　　　　　　　　　　　　　　(b)　　　　　　　　　　　　　　(c)

Figure 1. Photographs of specimens studied: (**a**) a sample of mammoth ivory from mammoth in Russia (Siberia); (**b**) a sample of ivory from adult Zimbabwean elephants; (**c**) Fluorapatite.

2.2. X-ray Diffraction

Part of the sample from the Retzius layer (Figure 2) was fractured into small lumps with an approximate size of $1.3 \times 1.3 \times 1.3$ cm. The texted planes include transverse planes (TP), circumferential planes (CP) and radial planes (RP). The other part was ground in an agate mortar and then sieved on 400-mesh screens. The packed powders were analyzed. This test was performed on a Smartlab X-ray diffractometer (Rigaku, Tokyo, Japan), equipped with a graphite monochromator, and using CuKα1 radiation at 45 kV and 200 mA. A divergent slit and a scatter slit, both of $1/6°$ width, were employed for the beam source. A receiving slit of 0.15 mm width was used for the detector. Data were collected in the high precision step-scan mode: $3°-80°$ 2θ range, $0.02°$ step size, and 1 s/step counting time. All the data were analyzed by the software Jade 6.5 (Jade, Christchurch, New Zealand).

2.3. Scanning Electron Microscope and Energy Dispersive Spectroscopy

The samples were fractured along the transverse planes (TP). The fracture surfaces with outermost layer (OL) and Retzius layer (RL) (Figure 2) were gold-coated and studied in a ZEISS SIGMA scanning electron microscope (15 KV) (ZEISS, Oberkochen, Germany), and samples were embedded by electric conductive adhesive in an aluminum plate under vacuum. Distribution of Ca, P, Mg, Na, Cl, C and Ca/P were obtained.
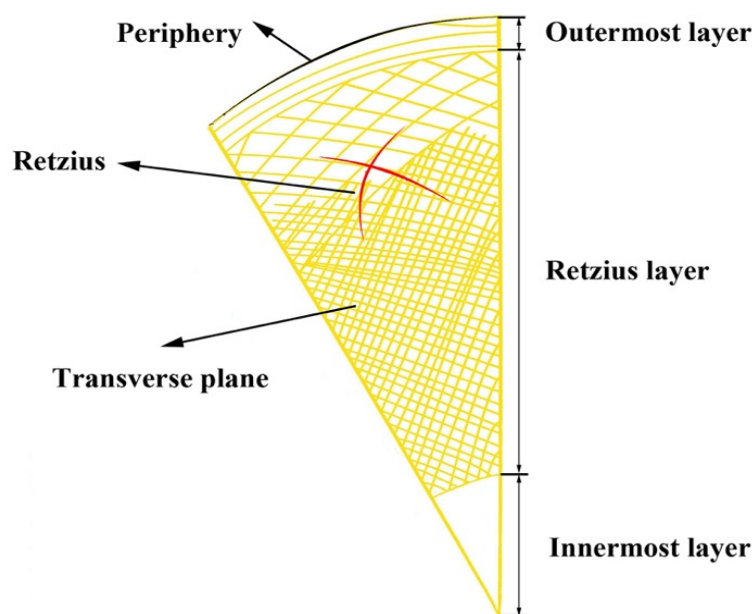
Figure 2. Schematic diagram of Retzius. This pattern consists of alternative lines interweaving to form a network, which begins at the center of the tusk and sweeps outwards to the periphery [17].

2.4. Infrared Spectrometry

A standard procedure was used for sample preparation. Samples with the weight of 2 ± 0.1 mg were added to 400 ± 1 mg KBr and then sieved on 200-mesh screens after they had been blended and ground in an agate mortar. They were dried at 120 °C overnight in an oven for the experiment. The IR spectra were recorded in transmittance mode with a Bruker Tensor II spectrometer (Bruker, Billerica, MA, USA). The sample includes the outermost layer (OL), Retzius layer (RL) and innermost layer (IL). Spectral scans at a spectral resolution of 4 cm^{-1} were accumulated over a period of about 120 s to give good signal-to-noise ratios. Reproducible spectra were obtained from several parts of each specimen.

3. Results and Discussion

3.1. Phase Identification

X-ray diffraction patterns in Figure 3a showed that the appearance of three main peaks at approximately 25.9° (d = 3.439 Å), 31.8° (d = 2.815 Å) and 32.2° (d = 2.779 Å) are consistent with the standard pattern of hydroxyapatite, indicating that the predominant inorganic phase of these samples is carbonate-substituted hydroxyapatite.

The refined structural parameters obtained for both species are presented in Figure 3b and Table 1. The cell parameters for the two studied samples are similar and slightly higher than standard hydroxyapatite. The a value is reported to be associated with the carbonate content and decreased with age, while the c value, associated with hydroxyl sites, is more stable [14].

Table 1. The cell parameters (a_0 and c_0) of ivory from an elephant and mammoth ivory.

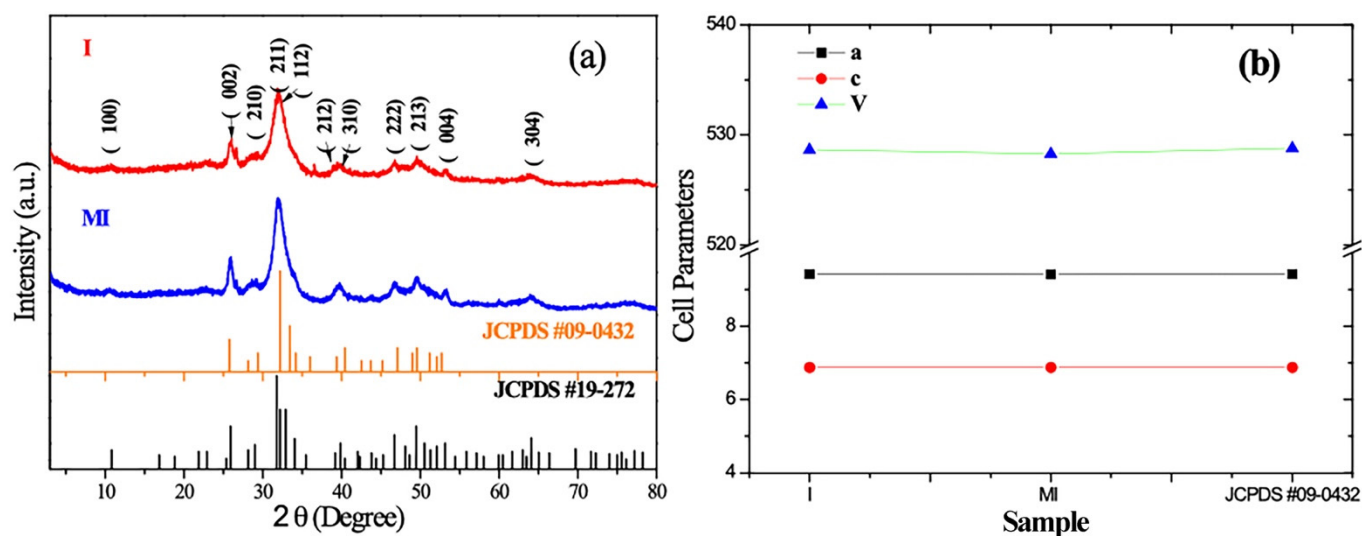|	a/Å	σ_a	c/Å	σ_c	V/Å^3	σ_V
I	9.4166	0.0195	6.8841	0.0006	528.65	1.0981
MI	9.4148	0.0178	6.8821	0.0006	528.29	0.9996
JCPDS #09-0432	9.418		6.884		528.8	

Figure 3. (**a**) The XRD patterns of mammoth ivory, ivory from elephant samples and standard profile of hydroxyapatite and carbonated hydroxyapatite (JCPDS #09-0432 and #19-272); (**b**) the cell parameters.

3.2. Elemental Analysis and Microstructure

Calcium–phosphate ratios (Ca/P) of stoichiometric hydroxyapatite, which is 1.67, are determined by geochemical phenomena. The Ca/P of samples studied, calculated from energy dispersive spectra (EDS), ranged between 1.37 and 1.47 in mammoth ivory and 1.20 and 1.27 in ivory from an elephant (Table 2), distinctly lower than the standard value, meaning the favorable biologically activity. The nucleation and growth stages of hydroxyapatite occur in a biological system containing various trace elements, and hydroxyapatite exchanges ions with its surroundings to optimize the biological functions. The element Ca is usually replaced by the elements with a similar radius (e.g., magnesium (Mg), sodium (Na)) [5]. Thus, we use the new Ca′ to do the calculation (Ca′ = Ca + Mg + Na). The Ca′/P value does not change significantly among the samples.

Table 2. EDS data of mammoth ivory and ivory from an elephant.

Title		w_B/%						Ca/P	Ca′/P
		C	O	Ca	P	Mg	Na		
MI	OL	36.9	37.4	13.8	7.8	1.0	0.4	1.37	1.60
	RL	32.9	42.5	14.6	7.7	0.7	0.4	1.47	1.65
I	OL	37.0	40.7	11.0	6.7	1.2	0.6	1.27	1.62
	RL	30.0	38.1	13.2	8.5	1.5	0.5	1.20	1.50

Ca/P, Ca′/P are calculated molar ratios; Ca′ = Ca + Mg + Na.

Through the Scanning Electron Microscope (SEM) images of the transverse plane (Figures 4a and 5a), both mammoth ivory and ivory from an elephant displayed lamellar structure, and the tabular nature of hydroxyapatite was observed, appearing regularly and tightly. In addition, the morphology of hydroxyapatite crystal may be recognized vaguely. The statistics of its size range and average size are shown in Figures 4b and 5b. The average sizes of both mammoth ivory and ivory from an elephant are similar, and the corresponding values are 29.25 and 28.15 nm, according to the estimation from Figures 4a and 5a. As a check, these values are calculated by the Scherrer equation below. The elemental mapping has been made to explore the elemental distribution, and the most widely distributed elements are C, O, Ca and P, which are the basic constituent elements of hydroxyapatite. In addition, Si, Al and K appeared almost in the same position in the mapping images and

implied the existence of kaolinite or other clay minerals here, which has not been reported before to our knowledge. However, further research is needed to explore the reason for the existence of clay minerals.
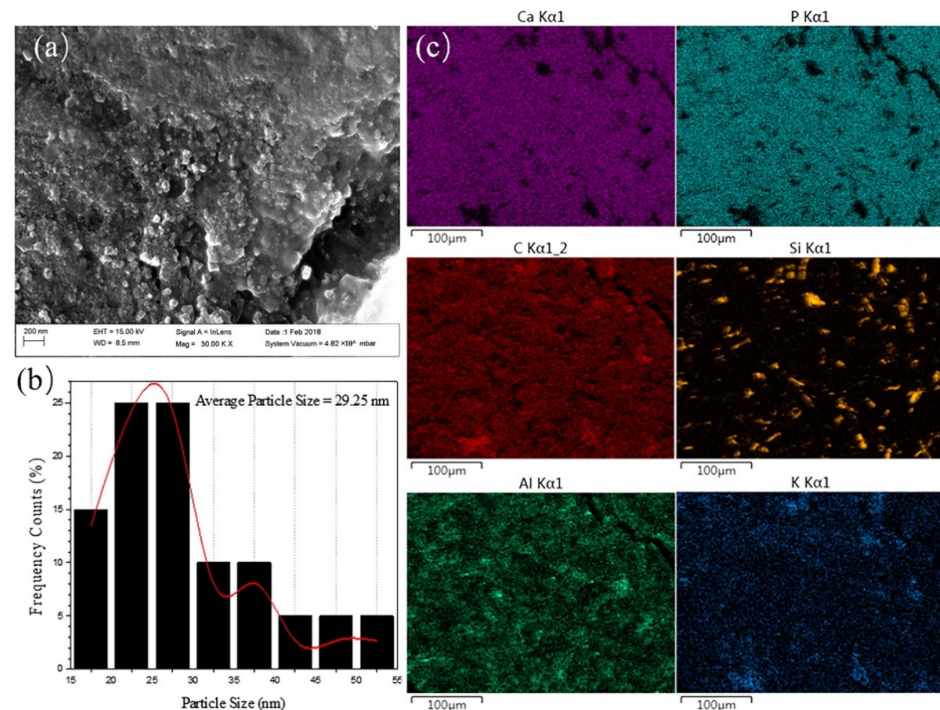

Figure 4. SEM image of the Retzius layer in transverse planes in mammoth ivory: (**a**) 200 nm magnification; (**b**) histogram of the particle size distribution drawn for 200 nm; (**c**) elemental mapping of the Retzius layer in mammoth ivory.

Figure 5. SEM image of the Retzius layer in transverse planes in ivory from an elephant: (**a**) 200 nm magnification; (**b**) histogram of the particle size distribution drawn for 200 nm; (**c**) elemental mapping of the Retzius layer in ivory from an elephant.
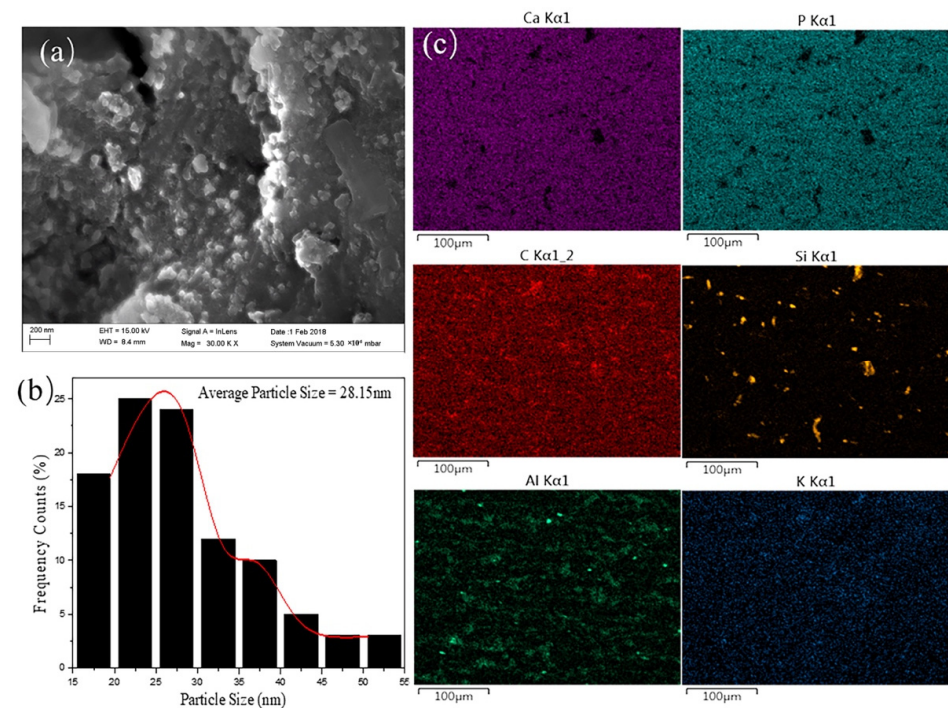
3.3. Infrared Spectroscopy

Infrared spectra of ivory consist of features clearly assignable to the inorganic matrix and organic protein components. The IR bands for all the samples except fluorapatite have been related to the PO_4 group, CO_3 groups at both B- and A-sites, and to OH according to the literature [20–23]. Specific decomposition procedures of complex IR bands into component bands are presented in Figure 6 and the assignments are listed in Table 3.
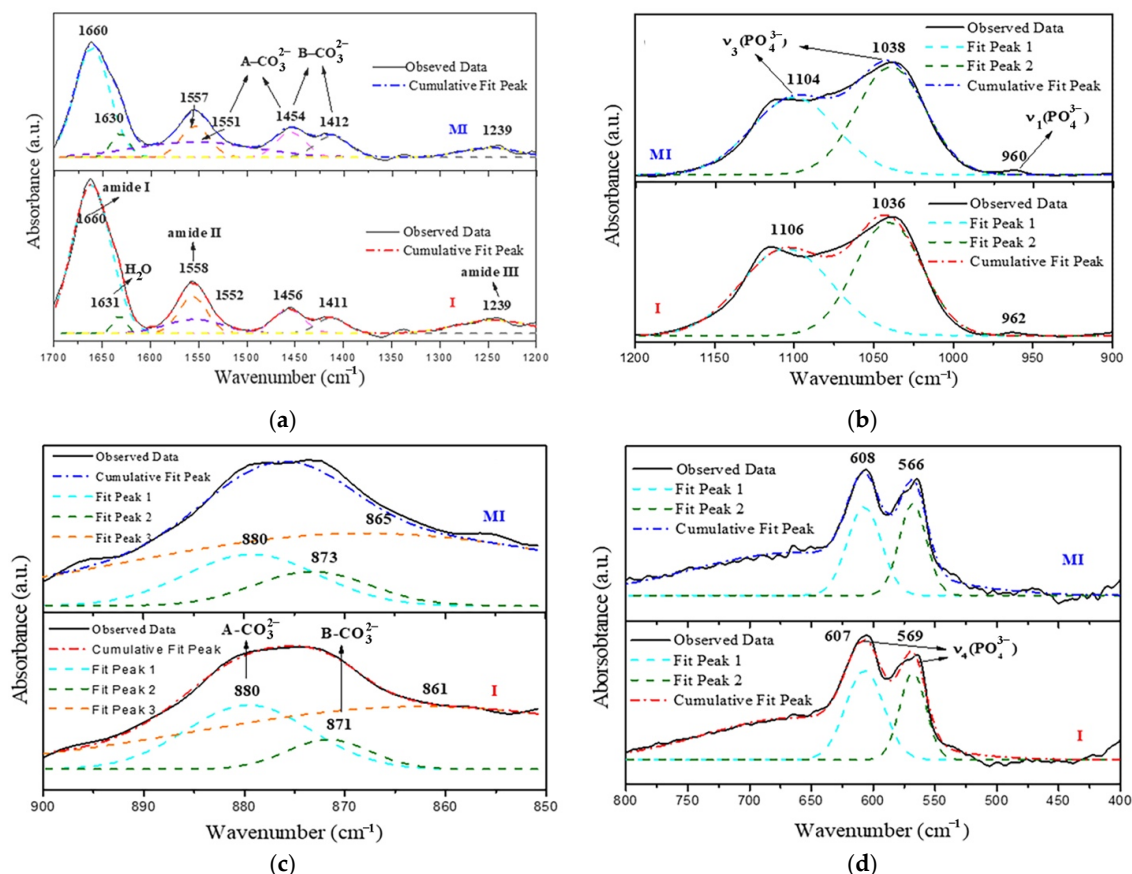

Figure 6. Infrared spectra of mammoth ivory and ivory from an elephant fitted by Gaussian functions with different wavenumber ranges (**a**) 1700~1200 cm^{-1}; (**b**) 1200~900 cm^{-1}; (**c**) 900~850 cm^{-1}; (**d**) 800~400 cm^{-1}.

1700~1200 cm^{-1} region: The broad band encountered in this region has been decomposed into seven Gaussian components (Figure 6a). CO_3^{2-} can replace both PO_4^{3-} (B-type) or OH (A-type) in hydroxyapatite. Three bands (1551, 1454, 1412 cm^{-1}) are related to the CO_3^{2-} group, which indicates that CO_3^{2-} substitution can simultaneously occur at the A- and B-site [25,26]. Amounts of CO_3^{2-} at the A- and B- site can be estimated by the area ratios under the Gaussian curves of A_{1551}/A_{566} and A_{1412}/A_{566} [27]. The area and the area ratios are listed in Table 4. Due to the higher value of A_{1551}/A_{566}, CO_3^{2-} occurs primarily at the A-site of hydroxyapatite in both mammoth ivory and ivory from an elephant. Three bands (1660–1670, 1550–1560, 1240 cm^{-1}) are related to amide I, II, III of collagen and the last one (1630 cm^{-1}) is related to H_2O. The relative intensities of collagen bands decrease slightly in mammoth ivory with respect to ivory from an elephant.

Table 3. Observed infrared band positions (cm^{-1}) of mammoth ivory and ivory from an elephant [24].

IR Absorption Bands	Positions (cm^{-1})	
	MI	**I**
ν(C=O) amide I	1660	1661
H$_2$O	1630	1631
δ(N-H); ν(C-H) amide II	1557	1558
ν_3 (CO)	1551 1454 1412	1552 1456 1411
δ(N-H); ν(C-N) amide III	1239	1239
ν_3 (PO)	1104 1038	1106 1036
ν_1 (PO)	960	959
ν_2 (CO)	880 873	880 871
ν_4 (PO)	608 566	607 569

Table 4. Areas and area ratios of IR bands of mammoth ivory and ivory from an elephant.

Bands		Mammoth Ivory		Ivory from an Elephant	
		cm^{-1}	Area	cm^{-1}	Area
ν_3 (C-O)	A	1551	6.35	1552	5.69
	B	1412	5.01	1411	3.28
ν_2 (C-O)	A	880	27.72	880	19.88
	B	873	8.56	872	11.53
ν_4 (P-O)		566	7.19	569	6.49
Area ratios	A_{1551}/A_{566}	0.883		0.877	
	A_{1412}/A_{566}	0.697		0.505	
	A_{880}/A_{566}	3.063		3.855	
	A_{873}/A_{566}	1.776		1.191	

900~850 cm^{-1} region: The band is decomposed into three Gaussian band components at 880, 873, 865 cm^{-1}, the former two of which are related to the CO$_3^{2-}$ group at the A- and B-site, respectively (Figure 6b). These two bands can also be used to assess the amount of CO$_3^{2-}$ and imply the conclusion as mentioned above. The band at 865 cm^{-1} has not been attributed to a specific site [28].

1200~900 cm^{-1} region and 800~400 cm^{-1} region: Three Gaussian band components decomposed in the 1200~900 cm^{-1} region and two in the 800~400 cm^{-1} region. These bands are all related to the vibration of phosphate.

3.4. Crystalline Characteristics
3.4.1. Crystal Size

Since the peak intensity in X-ray diffraction reflects the degree of crystal order or the perfection of a phase, the relative degree of crystallinity of hydroxyapatite was compared using the full width at half maximum (FWHM) of the (002) peak of different planes, and these two values are inversely proportional [29]. The FWHM of the (002) peak of different planes is shown in Figure 7 and Table 5, where all the values for the planes of mammoth ivory are lower than those for the corresponding planes of ivory from an elephant.
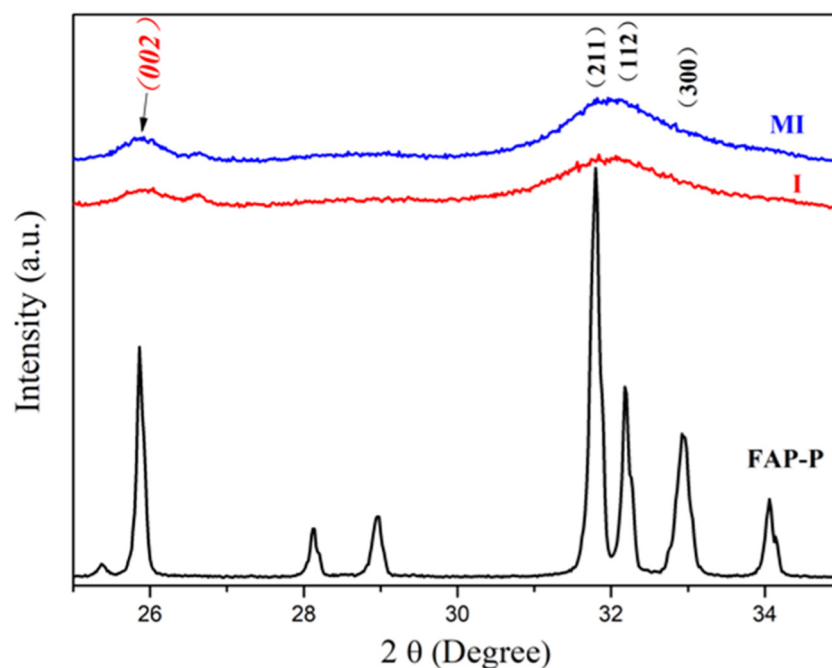
Figure 7. Comparison of (002) peak of mammoth ivory, ivory from an elephant and fluorapatite.

Table 5. The FWHM of the (002) peak of different planes and the domain thickness of the mammoth ivory and the ivory from an elephant.

		$\theta/(°)$	FWHM ((002))	β/rad	$L_{(002)}$/nm
Ivory from an elephant	TP	12.96	0.375	0.006545	21.50
	CP	12.96	0.399	0.006964	20.20
	RP	12.96	0.426	0.007435	18.92
Mammoth ivory	TP	12.94	0.348	0.006074	23.16
	CP	12.96	0.392	0.006842	20.56
	RP	12.96	0.395	0.006894	20.41

The crystal size measured in the direction perpendicular to the diffracting planes (002) was calculated using the Monshi–Scherrer equation [30].

$$\text{Ln } \beta = \text{Ln } (K\lambda/L) + \text{Ln } (1/\cos\theta) \tag{1}$$

where L is the crystal size in nanometers; $\lambda = 0.154056$ nm, which is the X-ray wavelength in nanometers; K is the Scherrer constant (here K = 0.89); β is equal to $B_{1/2}$-b, where $B_{1/2}$ is the experimental FWHM intensity of the diffraction peak (002), and b is the width of the same peak measured in highly crystalline hydroxyapatite as a standard; and θ is the diffraction angle for the diffraction peak (002). The calculated L values at the corresponding planes of the two species are shown in Table 5.

The degree of crystal disorder in hydroxyapatite is related to its crystal size. From the above-described results, the relative degree of crystallinity of hydroxyapatite in mammoth ivory appears to be higher than that in the ivory from an elephant. We further proposed that the difference between these two species may be related to the influence of the burial environment of the mammoth ivory in permafrost. The length dimensions of the individual crystals in mammoth ivory and ivory from an elephant are separately calculated to be 20.41–23.16 and 18.92–21.50 nm, respectively. These calculations were basically consistent with what we observed in 3.2. The FWHM and domain thickness indicated a poorly crystalline form of both biomaterials and a higher relative degree of crystallinity of hydroxyapatite in mammoth ivory.

3.4.2. Infrared Splitting Factor and Crystallinity

The degrees of splitting for the phosphate ion antisymmetric bending mode are determined by the weight fraction of crystalline hydroxyapatite; thus, crystallinity may be assessed using the infrared splitting factor (SF), which is based on the division of the phosphate antisymmetric bending mode into two peaks in the region of 560–605 cm^{-1} for these two phases [29,31–33]. Amorphous calcium phosphate gives a broad single absorption band in this region, while the anisotropic local electric field of crystalline apatite partially splits the degeneracy of this absorption band into a well-field doublet [34]. The comparison between the biomaterials and fluorapatite contributes to ensuring that there are no protein absorption bands in the SF region. In this method, a baseline is drawn from approximately 495–750 cm^{-1}. The heights of the 604 cm^{-1} (a) and 565 cm^{-1} (b) absorptions are summed and then divided by the height of the valley (c) between them (Figure 8), as shown below.
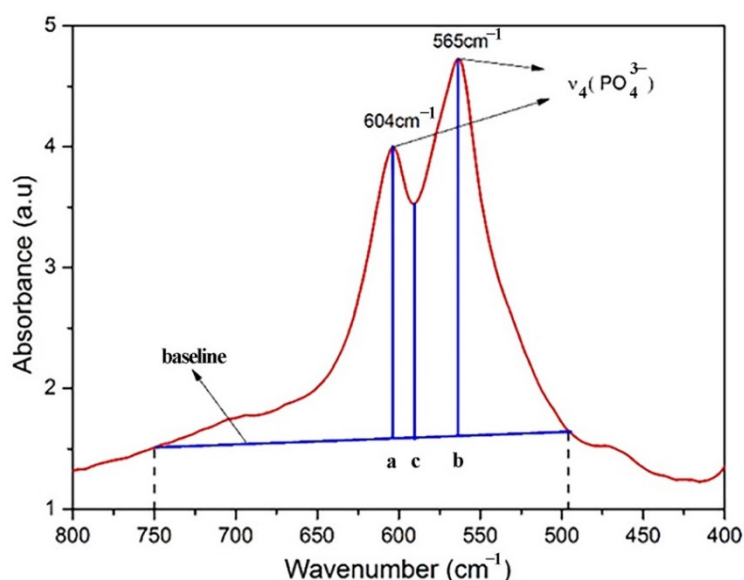
$$SF = (a + b)/c \qquad (2)$$

Figure 8. The portion of the infrared spectrum of sample I-R-2 used for calculating the crystallinity. Splitting factor (SF) measurement for the 600 cm^{-1} phosphate ion antisymmetric bending frequency in the calcium phosphate based on the calculation method of Weiner [33].

The results are given in Table 6, values obtained were found to be within a 2 percent error. We found the small SF values of mammoth ivory and ivory from an elephant (SF$_{MI-ave}$ = 2.87, SF$_{I-ave}$ = 3.17), both of which are far lower than geological mineral fluorapatite (SF$_{F-ave}$ = 20.5). Take fluorapatite as standard material and the crystallinity of which is considered as 10, then the crystallinity of mammoth ivory and ivory from an elephant is calculated as 1.55 and 1.4, respectively. However, the hydroxyapatite in mammoth ivory with crystal sizes slightly larger than that in ivory from an elephant had slightly higher SF values. Since the variation in SF was produced by fully crystalline hydroxyapatites [31], the results showed that the hydroxyapatite in mammoth ivory and ivory from an elephant are both in the form of weak crystallization, and the mammoth ivory contains more calcium phosphate in the crystalline hydroxyapatite than in the amorphous state.

Table 6. Spitting factor and crystallinity of mammoth ivory and ivory from an elephant.

Sample	Sample Number	SF	C
Ivory from an elephant	MI-IL	3.17	1.55
	MI-RL-1 *	3.23	1.58
	MI-RL-2 *	3.26	1.59
	MI-RL-3 *	3.12	1.52
	MI-RL-4 *	3.16	1.54
Mammoth Ivory	I-IL	1551	1.58
	I-RL-1 *	1454	1.59
	I-RL-2 *	1412	1.52
	I-RL-3 *	1239	1.54
Fluorapatite		20.5	10

* Note: RL-1~RL-4 means the different positions in the Retzius layer beginning at the center and sweeping outwards to the periphery, see Figure 2.

In addition, we also found a slight growth-dependent change in percentage crystallinity for the biomaterials, which implies the interrelation between the two phases of calcium phosphate in ivory growth. The fact that the innermost layer contains more amorphous than crystalline minerals suggests that amorphous calcium phosphate may be the first mineral deposited during the overall process of ivory formation and, moreover, the calcification process. This is not surprising because amorphous calcium phosphate appears prior to crystalline apatite in a synthetic system on a molecular level [35]. Therefore, there is a possibility that amorphous calcium phosphate can act as a metabolic precursor of crystalline hydroxyapatite in mammoth ivory and ivory from an elephant. The two-phased nature of bio-minerals may prove to be a valuable aid in understanding the molecular basis of the structure of mammoth ivory and ivory from an elephant.

4. Conclusions

This study revealed that microscopic crystalline hydroxyapatite and amorphous calcium phosphate are the main components of mammoth ivory and ivory from an elephant, of which the crystallinity was measured and compared. Refined cell parameters showed a similar value between mammoth ivory (a = 9.4148 Å and b = 6.8821 Å) and ivory (a = 9.4166 Å and c = 6.8841 Å). The estimated sizes of the individual crystals in mammoth ivory and ivory from an elephant are separately calculated to be 20.41–23.16 and 18.92–21.50 nm. CO_3^{2-} substitution has been explored by specific decomposition procedures of complex IR bands and it proves to occur primarily at the A-site of hydroxyapatite. The crystallinity of mammoth ivory and ivory from an elephant is largely lower than geological fluorapatite due to the bio-mineralization and mammoth ivory has a slightly higher crystallinity. Efforts to explore the relation between bio-mineralization and low crystallinity should be more fully exploited.

of Geosciences (Beijing) and the Institute of Geomechanics of the Chinese Academy of Geological Sciences are thanked.

References

1. Dove, P.M.; De Yoreo, J.J.; Weiner, S. *Biomineralization*; Mineralogical Society of America: Washington, DC, USA, 2003.
2. Mann, S. *Biomineralization: Principles and Concepts in Bioinorganic Materials Chemistry*, 1st ed.; Oxford University Press: Oxford, UK, 2001; pp. 6–12, discussion 24–37.
3. Cui, F.Z. *Biomineralization*, 1st ed.; Tsinghua University Press: Beijing, China, 2007.
4. Bale, W.F. A Comparative Röntgen-Ray Diffraction Study of Several Natural Apatites and the Apatite-like Constituent of Bone and Tooth Substance. *Am. J. Roentgenol.* **1940**, *43*, 735–747.
5. Hendricks, S.B.; Hill, W.L. The Nature of Bone and Phosphate Rock. *Proc. Natl. Acad. Sci. USA* **1950**, *36*, 731–737. [CrossRef] [PubMed]
6. Tanner, K.E. Small But Extremely Tough. *Science* **2012**, *336*, 1237–1238. [CrossRef] [PubMed]
7. Currey, J. The design of mineralised hard tissues for their mechanical functions. *J. Exp. Biol.* **1999**, *202*, 3285–3294. [CrossRef] [PubMed]
8. Robinson, R.A. An electron-microscopic study of the crystalline inorganic component of bone and its relationship to the organic matrix. *J. Bone Joint Surg.* **1952**, *34*, 389–435. [CrossRef] [PubMed]
9. Johansen, E.; Parks, H.F. Electron Microscopic Observations on the Three-Dimensional Morphology of Apatite Crystallites of Human Dentine and Bone. *J. Cell Biol.* **1960**, *7*, 743–746. [CrossRef]
10. Bocciarelli, D.S. Morphology of crystallites in bone. *Calcif. Tissue Res.* **1970**, *5*, 261–269. [CrossRef]
11. Jackson, S.A.; Cartwright, A.G.; Lewis, D. The morphology of bone mineral crystals. *Calcif. Tissue Res.* **1978**, *25*, 217–222. [CrossRef]
12. Weiner, S.; Price, P.A. Disaggregation of bone into crystals. *Calcif. Tissue Int.* **1986**, *39*, 365–375. [CrossRef]
13. Landis, W.J.; Song, M.J.; Leith, A.L.; Mc Ewen, L.; Mc Ewen, B.F. Mineral and Organic Matrix Interaction in Normally Calcifying Tendon Visualized in Three Dimensions by High-Voltage Electron Microscopic Tomography and Graphic Image Reconstruction. *J. Struct. Biol.* **1993**, *110*, 39–54. [CrossRef]
14. Neel, E.A.A.; Aljabo, A.; Strange, A.; Ibrahim, S.; Coathup, M.; Young, A.M.; Bozec, L.; Mudera, V. Demineralization–remineralization dynamics in teeth and bone. *Int. J. Nanomed.* **2016**, *11*, 4743–4763. [CrossRef] [PubMed]
15. Su, X.W.; Cui, F.Z. Hierarchical structure of ivory: From nanometer to centimeter. *Mater. Sci. Eng. C* **1999**, *7*, 19–29. [CrossRef]
16. Locke, M. Structure of Ivory. *J. Morphol.* **2008**, *269*, 423–450. [CrossRef] [PubMed]
17. Sun, X.Y.; He, M.Y.; Wu, J.L. Study of the Preferred Orientation of Hydroxyapatite in Ivory from Zimbabwe and Mammoth Ivory from Siberia. *Crystals* **2021**, *11*, 572. [CrossRef]
18. Su, X.W.; Cui, F.Z. Direct Observations on Apatite Crystals in Ivory. *J. Mater. Sci. Lett.* **1997**, *16*, 1198–1200. [CrossRef]
19. Rabiei, M.; Palevicius, A.; Dashti, A.; Nasiri, S.; Monshi, A.; Doustmohammadi, A.; Vilkauskas, A.; Janusas, G. X-ray Diffraction Analysis and Williamson-Hall Method in USDM Model for Estimating More Accurate Values of Stress-Strain of Unit Cell and Super Cells ($2 \times 2 \times 2$) of Hydroxyapatite, Confirmed by Ultrasonic Pulse-Echo Test. *Materials* **2021**, *14*, 2949. [CrossRef]
20. Holcomb, D.W.; Young, R.A. Thermal decomposition of human tooth enamel. *Calcif. Tissue Int.* **1980**, *31*, 189–201. [CrossRef]
21. LeGeros, R.Z. Apatites in biological systems. *Prog. Cryst. Growth Charact.* **1981**, *4*, 1–45. [CrossRef]
22. Young, R.A.; Wiles, D.B. Application of the Rietveld Method for Structure Refinement with Powder Diffraction Data. *Adv. X-ray Anal.* **1980**, *24*, 1–23. [CrossRef]
23. Farmer, V.C. *The Infrared Spectrum of Minerals*; Science Press: Beijing, China, 1982.
24. Rehman, I.; Smith, R.; Hench, L.L.; Bonfield, W. Structural evaluation of human and sheep bone and comparison with synthetic hydroxyapatite by FT-Raman spectroscopy. *J. Biomed. Mater. Res.* **1995**, *29*, 1287–1294. [CrossRef]
25. Vignoles, M.; Bonel, G.; Holcomb, D.W.; Young, R.A. Influence of preparation conditions on the composition of type B carbonated hydroxyapatite and on the localization of the carbonate ions. *Calcif. Tissue Res.* **1988**, *43*, 33–40. [CrossRef]
26. Ito, A.; Aoki, H.; Akao, M.; Teraoka, K.; Tsutsumi, S.; Onuma, K.; Tateishi, T. Hydrothermal Growth of Carbonate-containing Hydroxyapatite Single Crystals. *J. Cryst. Growth.* **1996**, *163*, 1311–1317. [CrossRef]
27. Michel, V.; Ildefonse, P.; Morin, G. Chemical and Structural Changes in Cervuselaphus Tooth Enamels during Fossilization (Lazaret Cave): A Combined IR and XRD Rietveld Analysis. *Appl. Geochem.* **1995**, *10*, 145–159. [CrossRef]
28. Rey, C.; Renugopalakrishnan, V.; Shimizu, M.; Collins, B.; Glimcher, M.J. A Resolution-enhanced Fourier Transform Spectroscopic Study of the Environment of the CO_3^{2-} ion in the Mineral Phase of Enamel during its Formation and Maturation. *Calcif. Tissue Int.* **1991**, *49*, 259–268. [CrossRef]
29. Sillen, A.; Sealy, J.C. Diagenesis of Strontium in Fossil Bone: A Reconsideration of Nelson et al. (1986). *J. Archaeol. Sci.* **1995**, *22*, 313–320. [CrossRef]
30. Rabiei, M.; Palevicius, A.; Monshi, A.; Nasiri, S.; Vilkauskas, A.; Janusas, G. Comparing Methods for Calculating Nano Crystal Size of Natural Hydroxyapatite Using X-Ray Diffraction. *Nanomaterials* **2020**, *10*, 1627. [CrossRef]

31. Termine, J.D.; Posner, A.S. Infrared Analysis of Rat Bone: Age Dependency of Amorphous and Crystalline Mineral Fractions. *Science* **1966**, *153*, 1523–1525. [CrossRef]
32. LeGeros, R.Z.; Tung, M.S. Chemical Stability of Carbonate- and Fluoride-Containing Apatites. *Caries Res.* **1983**, *17*, 419–429. [CrossRef] [PubMed]
33. Weiner, S.; Bar-Yosef, O. States of preservation of bones from prehistoric sites in the Near East: A survey. *J. Archaeol. Sci.* **1990**, *17*, 187–196. [CrossRef]
34. Stutman, J.M.; Termine, J.D.; Posner, A.S. Vibrational spectra and structure of the phosphate ion in some calcium phosphates. *Trans. N. Y. Acad. Sci.* **1965**, *27*, 669–675. [CrossRef]
35. Eanes, E.D.; Posner, A.S. Division of Biophysics Kinetics and Mechanism of Conversion of Noncrystalline Calcium Phosphate to Crystalline Hydroxyapatite. *Trans. N. Y. Acad. Sci.* **1965**, *28*, 233–241. [CrossRef]